Monthly Notices of the ROYAL ASTRONOMICAL SOCIETY

MNRAS **528,** 2026–2039 (2024) https://doi.org/10.1093/mnras/stae145
Advance Access publication 2024 January 13

Oxygen abundance of γ Vel from [O III] 88 μm *Herschel*/PACS spectroscopy

Paul A. Crowther [1★] M. J. Barlow [2] P. Royer,[3] D. J. Hillier [4] J. M. Bestenlehner [1] P. W. Morris [5] and R. Wesson [6]

[1]*Department of Physics and Astronomy, University of Sheffield, Sheffield S3 7RH, UK*
[2]*Department of Physics and Astronomy, University College London, Gower Street, London WC1E 6BT, UK*
[3]*Institute of Astronomy, KU Leuven, Celestijnenlaan 200d - box 2401, B-3001 Leuven, Belgium*
[4]*Department of Physics and Astronomy & Pittsburgh Particle Physics, Astrophysics and Cosmology Center (PITT PACC), University of Pittsburgh, 100 Allen Hall, 391 O'Hara St, Pittsburgh, PA 15260, USA*
[5]*California Institute of Technology, IPAC M/C 100-22, 770 S Wilson Ave, Pasadena, CA 91125, USA*
[6]*School of Physics and Astronomy, Cardiff University, Queen's Buildings North Building, 5 The Parade, Newport Road, Cardiff CF24 3AA, UK*

Accepted 2024 January 11. Received 2024 January 10; in original form 2023 August 11

ABSTRACT

We present *Herschel* PACS spectroscopy of the [O III] 88.4 μm fine-structure line in the nearby WC8+O binary system γ Vel to determine its oxygen abundance. The critical density of this line corresponds to several $10^5 R_*$ such that it is spatially extended in PACS observations at the 336 pc distance to γ Vel. Two approaches are used, the first involving a detailed stellar atmosphere analysis of γ Vel using CMFGEN, extending to $N_e \sim 10^0$ cm^{-3} in order to fully sample the line formation region of [O III] 88.4 μm. The second approach involves the analytical model introduced by Barlow et al. and revised by Dessart et al., additionally exploiting *ISO* LWS spectroscopy of [O III] 51.8 μm. We obtain higher luminosities for the WR and O components of γ Vel with respect to De Marco et al., log L/L$_\odot$ = 5.31 and 5.56, respectively, primarily due to the revised (higher) interferometric distance. We obtain an oxygen mass fraction of $X_O = 1.0 \pm 0.3$ per cent for an outer wind volume filling factor of $f = 0.5 \pm 0.25$, favouring either standard or slightly reduced Kunz et al. rates for the $^{12}C(\alpha, \gamma)^{16}O$ reaction from comparison with BPASS binary population synthesis models. We also revisit neon and sulphur abundances in the outer wind of γ Vel from *ISO* SWS spectroscopy of [S IV] 10.5 μm, [Ne II] 12.8 μm, and [Ne III] 15.5 μm. The inferred neon abundance $X_{Ne} = 2.0^{+0.4}_{-0.6}$ per cent is in excellent agreement with BPASS predictions, while the sulphur abundance of $X_S = 0.04 \pm 0.01$ per cent agrees with the solar abundance, as expected for unprocessed elements.

Key words: stars: abundances – stars: early-type – stars: massive – stars: Wolf–Rayet – infrared: stars.

1 INTRODUCTION

The majority of oxygen and other α-elements in the Universe are created in massive stars. Such stars not only achieve requisite temperatures to synthesize heavy elements, but during late evolutionary phases inject immense mechanical energy to mix these fresh ingredients into the interstellar medium (ISM). Wolf–Rayet (WR) stars are the evolved descendants of O-stars that exhibit prodigious mass-loss rates of $\sim 10^{-5}$ M$_\odot$ yr^{-1} via line-driven winds, and are characterized by strong emission line spectra of nitrogen (WN), carbon (WC), or oxygen (WO), representing a broad evolutionary sequence (Crowther 2007). Evidence for chemical enrichment of the ISM by WR winds has been observed in the circumstellar nebulae of individual WR stars (Esteban et al. 1992; Stock, Barlow & Wesson 2011), and invoked to explain an increased N/O ratio in galaxies displaying WR spectral features (Brinchmann, Kunth & Durret 2008; López-Sánchez & Esteban 2010).

WC (and WO) stars represent the final evolutionary stages of $M_{ini} \gtrsim 20$ M$_\odot$ stars (Meynet & Maeder 2005). Following a lifetime of extreme mass-loss, these 'naked' helium stars offer a unique window into the chemical evolution of massive star cores. Accurate measurement of abundances in such stars stars can therefore provide important constraints on nuclear reaction rates and the efficiency of various internal mixing processes.

The precise amount of oxygen produced in massive stars has long been a contentious issue (Fowler 1984). The ratio $^{12}C/^{16}O$ is sensitive to the core density and temperature and duration of helium burning, but it depends directly on the competition in rates of the $3\alpha \rightarrow {}^{12}C$ and $^{12}C(\alpha, \gamma)^{16}O$ processes. The rate of $3\alpha \rightarrow {}^{12}C$ is reasonably secure (Fynbo et al. 2005), but a significant level of uncertainty remains regarding the rate of $^{12}C(\alpha, \gamma)^{16}O$ (Buchmann & Barnes 2006). Aadland et al. (2022) have recently discussed implications of varying rates for contemporary evolutionary models of massive stars.

The abundances of helium and carbon in WC atmospheres are well known. Model atmosphere codes such as CMFGEN (Hillier & Miller 1998) and POWR (Gräfener, Koesterke & Hamann 2002) have been developed to solve the transfer equation under non-local

★ E-mail: paul.crowther@sheffield.ac.uk

thermodynamic equilibrium (LTE) conditions in an expanding, spherically symmetric, clumpy atmosphere. These have been applied to reproduce the plethora of carbon recombination lines in WC near-ultraviolet (UV)/optical/near-infrared (IR) spectra, typically revealing C/He = 0.1–0.4 by number (X_C = 20–50 per cent by mass) (Crowther et al. 2002; Sander, Hamann & Todt 2012; Aadland et al. 2022).

Despite the prevalence of oxygen lines in WC and particularly WO spectra, the measurement of abundances by spectroscopic modelling has been challenging, since C lines dominate most regions of the UV–optical spectrum, and many O features are highly sensitive to ionization (Crowther et al. 2002). The O lines most appropriate and commonly used to determine abundances in WC spectra are found in the near-UV (3000–3500 Å), and are therefore severely affected by dust extinction in the Galactic plane. Using space-based UV observations of WC and WO stars in the Large Magellanic Cloud (LMC), Aadland et al. (2022) measure oxygen abundances of O/He = 0.01–0.05 by number (X_O = 2–9 per cent by mass). Another problem has been the complexity of model atoms required to accurately compute radiative transfer solutions in the winds of WC and WO stars, particularly for late-type WC stars abundant in C^+ and C^{2+}. Williams, Crowther & van der Hucht (2015) presented O abundance determinations in WC9 stars, based on CMFGEN model atmosphere analyses of optical spectra, obtaining O/He = 0.005–0.017(X_O = 2–4 per cent by mass).

A more straightforward indicator of elemental abundance is provided by forbidden fine-structure lines that originate at low electron densities, corresponding to very large radii $> 10^3\,R_*$, where R_* is the radius with Rosseland optical depth ∼10. The flux in these lines is directly proportional to the fractional abundance (γ_i) of the emitting ionic species (Barlow, Roche & Aitken 1988). However, this method requires knowledge of the mass-loss properties and ionization structure. This approach has been adapted for clumped winds by Dessart et al. (2000), who use mid-IR *ISO* SWS spectroscopy of neon and sulphur lines to calculate ionic abundances of these elements in WC stars (see also Morris et al. 2000). The mid-IR *Spitzer* IRS spectrograph has also been used to study ionic abundances in WN and WC stars (Morris, Crowther & Houck 2004; Crowther et al. 2006).

Fine splitting in the ground state of O^{2+} generates the [O III] 88.36 μm ($^3P_1 - {}^3P_0$) forbidden fine-structure line. With a critical density[1] of $N_{\rm crit}$∼500 cm^{-3} (Rubin 1989), this line is expected to originate from radii of a few $\times\,10^5\,R_*$ in WC stars. *Herschel*'s Photoconductor Array Camera and Spectrometer (PACS) permits observation of Galactic WC stars at [O III] 88.36 μm, from which we aim to provide an independent oxygen abundance.

This paper is focused on [O III] 88.4 μm PACS observations of γ Vel (WR11, HD 68273).[2] At an interferometric distance of 336^{+8}_{-7} pc (North et al. 2007; van Leeuwen 2007), this is comfortably the closest WR star (Rate & Crowther 2020). γ Vel is a WC8+O binary system with a 78.5 d (Niemela & Sahade 1980), moderately eccentric orbit (North et al. 2007). It has been extensively studied across the electromagnetic spectrum including X-rays (Skinner et al. 2001; Schild et al. 2004), UV (Stecher 1970; St.-Louis, Willis & Stevens 1993), optical (Schmutz et al. 1997), near-IR (Aitken, Roche & Allen 1982), mid-IR (Barlow, Roche & Aitken 1988; van der Hucht et al. 1996), and mm/radio (Seaquist 1976; Williams et al. 1990; Chapman et al. 1999). De Marco & Schmutz (1999) and De Marco et al. (2000) have determined dynamical masses for its components of 30 $M_\odot$ (O) and 9 $M_\odot$ (WC8), adopting the original *Hipparcos* distance of ∼258 pc (Schaerer, Schmutz & Grenon 1997; de Zeeuw et al. 1999). Its age is 5.5 ± 1 Myr (Eldridge 2009) and is located within a self-named stellar cluster within the Vela OB2 association (Jeffries et al. 2009, 2017; Franciosini et al. 2018).

In order to determine the oxygen abundance from fine-structure lines, it is necessary to determine the outer WC wind properties. It is firmly established that the inner winds (1–10 R_*) of hot, luminous stars are clumped, likely as a consequence of intrinsic instability in the line driving mechanism (Owocki & Rybicki 1984). This explains many observational features unaccounted for by homogeneous wind models, such as the strength of electron scattering wings in WR spectra (Hillier 1991). For WR stars, consistency with observations has most commonly been found for inner wind clumping with volume filling factor $f \simeq 0.1$ (Morris et al. 2000; Kurosawa, Hillier & Pittard 2002). However, the radial extent to which clumping persists and whether the filling factor remains constant is unknown, but there is both theoretical and observational evidence to suggest that it varies with radius.

Runacres & Owocki (2002) performed 1D simulations of a line-driven hot-star wind out to 100 R_*. A highly structured wind is generated, consisting of strong reverse shocks and weaker forward shocks confining high-density regions, separated by high-speed rarefied material. They find that collisions of these dense regions allow structure to persist up to the largest radii considered, with the so-called clumping factor (1/f) rising to a maximum of ∼10 around 20 R_* and falling to ∼5 at and beyond 50 R_*. As an extension to these simulations, Runacres & Owocki (2005) take advantage of the diminishing radiative force beyond ∼30 R_* to analyse the evolution wind structure out to 1300 R_* in a purely hydrodynamical sense. Once again, persistent structure is seen out to the largest radii, characterized by a clumping factor ∼4 (f ∼ 0.25) between 300 and 1300 R_*. Sundqvist, Owocki & Puls (2018) extend simulations to 2D, revealing somewhat lower clumping factors.

Variations in wind clumping are also observationally based, by the discrepancy in mass-loss rates derived using diagnostics originating from different depths in a stellar wind. For example, Puls et al. (2006) reveal a factor of two difference between H α derived $\dot{M}$ (≤ 2 R_*) and radio derived $\dot{M}$ (∼ 100 R_*) in O supergiants under the assumption of constant clumping factor, implying a lower clumping factor in the radio-emitting region. Najarro, Hanson & Puls (2011) utilized mid-IR spectroscopy of O stars to quantify the radial dependence of clumping, obtaining f = 0.17 for ζ Pup (O4 If) at ∼ 100 R_*, while Rubio-Díez et al. (2022) favour volume filling factors of f = 0.25–0.5 for OB supergiants from far-IR photometry.

In Section 2, we provide details of the observational data sets used. Section 3 details a spectroscopic analysis of γ Vel including fits to mid- and far-IR fine-structure lines of oxygen, neon, and sulphur. We summarize the analytical method of Barlow, Roche & Aitken (1988) in Section 4 and apply this to γ Vel in order to calculate oxygen, neon, and sulphur abundances, informed by our spectroscopic analysis. Comparisons between our derived oxygen abundance and evolutionary predictions are provided in Section 5 and brief conclusions are drawn.

2 OBSERVATIONS

2.1 *Herschel* PACS spectroscopy

γ Vel was observed with the Photodetector Array Camera and Spectrometer (PACS, Poglitsch et al. 2010) instrument onboard the

[1] $N_{\rm cric}$ is the density at which an energy level is depopulated equally by collisions and spontaneous emission (Osterbrock & Ferland 2006).

[2] This system is commonly referred to as γ^2 Vel, but at V = 1.83 mag, is significantly brighter than γ^1 Vel (HD 68243), another early-type binary with V = 4.17 mag, so we favour γ Vel or γ Vel A for the WR+O system.

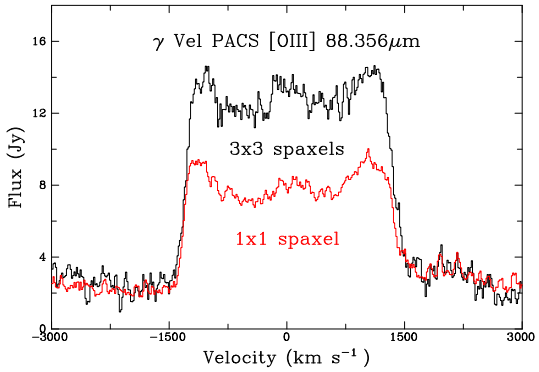

Figure 1. PACS spectroscopy of [O III] 88.4 μm fine-structure line in γ Vel, extracted from 3 × 3 central spaxels (black) versus central spaxel, highlighting its spatial extent $\gtrsim$1.5 spaxels, i.e. $\gtrsim$4500 au.

Herschel Space Telescope on 2012 December 7 in spectroscopy mode (P.I. Crowther). PACS images a field of view of 47 arcsec × 47 arcsec, resolved into a grid of 5 × 5 spectroscopic pixels, or 'spaxels', each spanning 9.4 arcsec × 9.4 arcsec. This field of view is rearranged via an image slicer on to two 16 × 25 Ge:Ga detector arrays, providing simultaneous first-order 105–210μm (R ∼1000–2000) and second-order 55–105μm (R ∼1500–3000) spectroscopy.

Scans totalling 2383 s covering 86.2–90.1μm with high spectral sampling density were carried out for γ Vel. This wavelength range corresponds to ±5000 km s^{-1}. The 88 μm line was observed in second order (R ∼ 2500) in chopping/nodding mode with a small chopper throw, and an additional window was simultaneously observed at 176 μm in first order. The first (second) order data sets were reduced using *Herschel* Interactive Processing Environment (HIPE) 10.0.1496 (10.0.1297) and calibration set 45. We apply standard point source corrections (PSCs) to the central spaxel in both instances, but prefer the integral over the central nine spaxels for the second order data set (excluding PSC) as discussed below.

For our adopted distance of 336^{+8}_{-7} pc to γ Vel, the 9.4 arcsec spaxel scale of PACS corresponds to ∼3000 au. The critical density of 88 μm occurs at a radius of 2 × 10^5 R_* (∼ 2000 au) for R_* ∼ 1.7 $R_\odot$ (Section 3). Therefore, the physical scale of the emitting region, may be resolvable by PACS for γ Vel. Indeed, in Fig. 1 we show the PACS scan, revealing 88.4 μm line emission extending beyond the central spaxel, confirming the physical extension of the emitting region as $\gtrsim$ 1.5 spaxels, i.e. 4500 au. The total [O III] 88.4 μm line flux is (3.4 ± 0.5) × 10^{-12} erg s^{-1} cm^{-2}, accounting for the 15 per cent absolute flux calibration uncertainties of PACS.[3] It also displays a measurable continuum flux, both adjacent to [O III] in second order (2.4 ± 0.6 Jy) and at 176 μm in first order (1.5 ± 0.3 Jy). As anticipated, no spectral features are detected in first order. Roche, Colling & Barlow (2012) have previously spatially resolved the outer wind of γ Vel from ground-based mid-IR observations of [S IV] and [Ne II] fine-structure lines.

Forbidden fine-structure lines provide the most direct means of measuring terminal wind velocities in WR stars, as they originate entirely from the asymptotically flowing region of the stellar wind (Barlow, Roche & Aitken 1988). Since the line is optically thin, it is expected to have a flat-topped and rectangular profile. [O III] 88.4 μm exhibits structure within the flat-topped profile, although this is reminiscent of [Ne III] 15.5 μm observations of γ Vel from *ISO*-SWS (Dessart et al. 2000). The full width of the emission line should therefore correspond to twice v_∞. However, in reality, the line profile will be modified by the instrumental profile, making emission lines slightly non-rectangular. We adopt the full width at zero intensity (FWZI) as twice v_∞. We obtain $v_\infty = 1500 \pm 20$ km s^{-1} from [O III] 88.36 μm, in good agreement with previous fine-structure (Barlow, Roche & Aitken 1988), near-IR (Eenens & Williams 1994), and UV (Prinja, Barlow & Howarth 1990) velocities of 1520, 1450, and 1460 km s^{-1}, respectively, the latter obtained from the blue absorption edge of the UV P Cygni C IV 1550 Å profile.

[3] https://www.cosmos.esa.int/documents/12133/996891/PACS+Explanatory+Supplement

2.2 Archival UV/optical spectroscopy

Extensive archival UV/optical spectroscopy of γ Vel exists, including *Copernicus* (Johnson 1978), *IUE* (St.-Louis, Willis & Stevens 1993), and ESO 0.5m HEROS (Schmutz et al. 1997). *Copernicus* far-UV and near-UV spectroscopy covers λλ946–3175 at a resolution of 0.2–0.4 Å, while high resolution *IUE* spectroscopy with the SWP and LWR cameras cover 1150–3300 Å. We have utilized calibrated *IUE* observations at phase 0.5 (St.-Louis, Willis & Stevens 1993), plus far-UV *Copernicus* U2 spectroscopy from 1977 March, although no official flux calibration exists for the latter. The H I column density towards γ Vel is log N(H I) = 19.8 cm^{-2} according to Bohlin (1975) and York & Rogerson (1976).

In the optical, Aller & Faulkner (1964) discuss the optical morphology of γ Vel. We use phase-averaged ESO 0.5 m HEROS spectroscopy covering 0.35–0.55 μm and 0.58–0.86 μm (Schmutz et al. 1997; De Marco & Schmutz 1999). Since these were not flux calibrated, we utilize relative intensities of optical emission lines from Aller & Faulkner (1964) to produce a relatively calibrated optical spectrum for the 0.4–0.55 μm HEROS data set, which is put on an absolute scale via narrow-band magnitudes b = 1.42 and v = 1.70 (De Marco et al. 2000). Violet and red HEROS data set is anchored to the composite continua of the O+WC8 model. We prefer narrow-band filter optical magnitudes to standard broad-band photometry (Johnson et al. 1966) owing to emission line contamination of the latter. Since HEROS coverage excludes the C III λ5696 and C IV λ5808 classification lines, we note F_{5696}/F_{5808} = 1.4 according to Aller & Faulkner (1964).

Since γ Vel is a binary system, we adopt a flux ratio of F_v(O)/F_v(WC8) = 3.61 following De Marco et al. (2000), i.e. M_v(WC8) –M_v(O) = +1.39 mag. Using our adopted distance modulus (7.63 mag) and extinction of E_{B-V} = 0.09 mag imply a systemic absolute magnitude of M_v = –6.24 mag, with M_v(O) = –5.97 mag and M_v(WC8) = –4.58 mag. The relative contribution of its constituents will vary with wavelength, with O to WR continuum light ratios of 3.7 at 0.5 μm and 1.0 at 2.0 μm (De Marco & Schmutz 1999).

2.3 Archival IR spectroscopy

Barnes, Lambert & Potter (1974) and Aitken, Roche & Allen (1982) present near-IR spectroscopy of γ Vel, supplemented by He I 1.083 μm spectroscopy from ESO's New Technology Telescope (NTT)+EMMI (De Marco et al. 2000). IR photometry between 1 and 13 μm is obtained from average measurements by Williams et al. (1990), supplemented by bands 3–4 from *WISE* (Wright et al. 2010). *ISO* SWS (de Graauw et al. 1996) mid-IR spectroscopy covering 2.4–27.5 μm (R = 820–1700) includes a mix of inner wind and fine-structure lines and has been discussed by van der Hucht et al. (1996). *ISO* LWS (Clegg et al. 1996) far-IR spectroscopy (PI M.J.

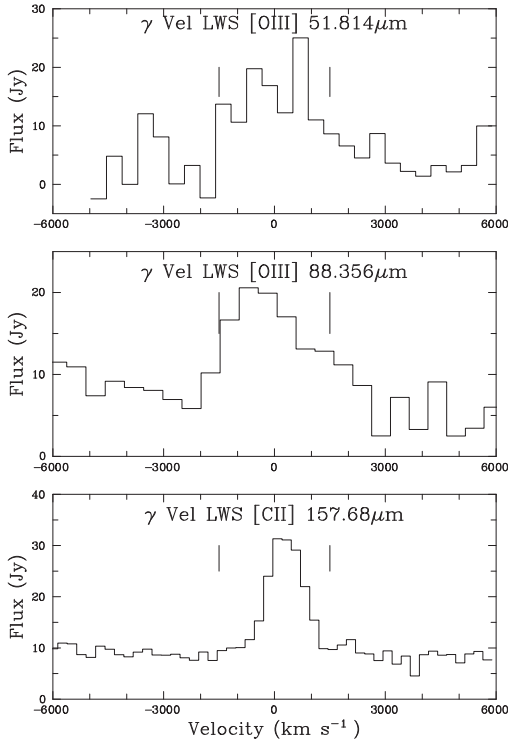

Figure 2. *ISO*-LWS spectrum of γ Vel, an average of back and forth scans, plotted in velocity space about a central wavelength [O III] 51.81μm (top), [O III 88.36 μm (centre), and [C II] 157.68 μm (bottom). Vertical lines indicate the expected extent of the stellar wind $v_\infty = 1500$ km s^{-1}.

Barlow) obtained from the *ISO* archive[4] cover 43–197 μm. γ Vel suffers from low S/N in the long wavelength SWS (30–45 μm) and short wavelength LWS (43–90 μm) channels of *ISO*. Nevertheless, we have been able to use the average fluxed spectra of back and forth scans to identify several fine-structure lines [O III] 51.81 μm, 88.36 μm, and [C II] 157.7 μm, as shown in Fig. 2.

The *ISO* [O III] 51.81μm spectrum of γ Vel is very noisy, posing a problem for the measurement of line flux as the continuum level is difficult to determine. We measure the flux of this line in two ways; first using the FLUX command from the Starlink spectroscopic package DIPSO (Howarth et al. 2004) between the expected velocity limits after subtraction of a by-eye estimate of the continuum, and second by fitting a Gaussian profile to the line using DIPSO's emission line fitting (ELF) suite, after subtraction of a (second order) polynomial fit to the continuum. Although the emission line is expected to be flat-topped and highly non-Gaussian, this structure is lost in the noise, permitting us to employ Gaussian fitting as an approximation. From the FLUX method, multiple measurements give an average [O III] 51.81 μm line flux of $(8.1 \pm 0.6) \times 10^{-12}$ erg s^{-1}cm^{-2}, and the Gaussian fit gives a compatible $(7.8 \pm 1.6) \times 10^{-12}$ erg s^{-1}cm^{-2}. We adopt a line flux of $(8 \pm 1) \times 10^{-12}$ erg s^{-1}cm^{-2}, incorporating 10 per cent flux calibration uncertainties for 'medium' point sources (García-Lario 2000).

The 84–93 μm region is covered by the first order of LW1 detector of *ISO* LWS, as well as second order of the SW5 detector. The standard data product adopts the higher resolution SW5 spectrum, but LW1 has significantly higher sensitivity permitting [O III] 88.36 μm to be detected (Fig. 2). The integrated flux measured using DIPSO'S ELF package is $(4.2 \pm 0.4) \times 10^{-12}$ erg s^{-1}cm^{-2}, 20 per cent higher than the *Herschel* PACS measurement. We favour the latter in our analysis owing to its improved S/N and order of magnitude improved spectral resolution. Finally, [C II] 157.68 μm is prominent in the long wavelength LWS channel. This line has a flux of $(1.84 \pm 0.08) \times 10^{-12}$ erg s^{-1}cm^{-2}, although it is spectrally unresolved since its full width at half-maximum matches the *ISO*-LWS grating resolution of $R \sim 260$, so does not arise in the stellar wind (its critical density is $\sim$50 cm^{-3}).

[4] http://iso.esac.esa.int/ida/

3 SPECTROSCOPIC ANALYSIS

The detailed spectral analysis of the O and WC components in γ Vel by De Marco & Schmutz (1999) and De Marco et al. (2000) form the basis of our study. We utilize the non-LTE line-blanketed model atmosphere code CMFGEN (Hillier & Miller 1998) that solves the radiative transfer equation in the co-moving frame, subject to statistical and radiative equilibrium, assuming an expanding, spherically symmetric, homogenous, or clumped, time-independent atmosphere. Line blanketing is treated correctly in the transfer problem except that a 'super level' approach is used, involving the combining of levels with similar energies and properties into a single super level.

3.1 O star

For the O star component of γ Vel we include the following elements: H, He, C, N, O, Ne, Na, Mg, Al, Si, P, S, Ca, Fe, and Ni, with standard Milky Way abundances. We adjust the physical parameters obtained by De Marco & Schmutz (1999) to the modern distance of 336 pc, but otherwise do not attempt to revise its solution, since our focus is on the outer wind of the WC star. Nevertheless, we note that the composite WC+O HEROS spectroscopy favours a high rotation rate of $v_{\rm eq} \sin i \sim 350$ km s^{-1} for the O star from comparison with He I λ4471 (Schmutz et al. 1997, their fig. 5), somewhat higher than the previous estimate of $v_{\rm eq} \sin i \sim 220$ km s^{-1} (Baade, Schmutz & van Kerkwijk 1990). High rotation velocities are expected for the mass gainer in a post-mass transfer system (de Mink et al. 2013). We use a hydrostatic solution at depth, together with a standard $\beta = 1$ law for the wind, and adopt a smooth wind (the IR energy distribution of γ Vel is dominated by the WC component). The outer boundary of the O star model is set at 200 R_*, corresponding to $N_{\rm e} = 5 \times 10^4$ cm^{-3} and $T_{\rm e} = 9500$ K. Physical and wind properties are summarized in Table 1.

3.2 WC8 star

For the WC component of γ Vel we include the following elements: He, C, O, Ne, Si, S, Ar, Ca, Fe, and Ni. Intermediate-mass elements (Ar, Ca) are included since they have a strong influence on the extreme UV blanketing (complementing Fe, Ni) that affects the strength of key optical diagnostics including C III λ5696, such that higher temperatures are necessary to reproduce optical diagnostic lines (C III λ5696, C IV λλ5801–12) with respect to previous studies (De Marco et al. 2000).

For the velocity law, we use a hydrostatic solution at depth, together with a standard $\beta = 1$ for the outer wind. We adopt a turbulent velocity of 100 km s^{-1}, requiring $v_\infty = 1420$ km s^{-1} in order to reproduce the mid-IR fine-structure lines. The emerging consensus is that clumping persists to large radii (at least 10^3 R_*) in a line-driven wind, characterized by a clumping (volume filling) factor that disperses to a minimum of 4–5 ($f = 0.2$–0.25) according to Runacres

Table 1. Physical, wind, and chemical parameters for the WC8 and O7.5 III components of γ Vel from CMFGEN analysis, updated from De Marco & Schmutz (1999) and De Marco et al. (2000). These include radially dependent volume filling factors, $f_{\log N_e}$, for the WC8 component at various electron densities (N_e/cm^{-3}), corresponding to the line-forming regions of optical lines, mid-IR (e.g. [Ne III] 15.5 μm), and far-IR (e.g. [O III] 88 μm) fine-structure lines, respectively.

Star	T_* (kK)	$T_{\rm eff}$ (kK)	R_* ($R_\odot$)	$\log g$ (cm s^{-2})	$\log L$ ($L_\odot$)	v_∞ (km s^{-1})	$\log(\dot{M})$ ($M_\odot$ yr^{-1})	$R_{\rm max}$ (R_*)	f_{12}	f_5	f_0	$M_{\rm v}$ (mag)	$X_{\rm H}$ (per cent)	$X_{\rm He}$ (per cent)	$X_{\rm C}$ (per cent)	$X_{\rm N}$ (per cent)	$X_{\rm O}$ (per cent)	$X_{\rm Ne}$ (per cent)	$X_{\rm S}$ (per cent)	$X_{\rm Fe}$
WC8	90	47.5	1.9	4.85	5.31	1420	−4.84	4.5×10^6	0.1	0.5	0.5	−4.6	0	67	30	0	1.1	1.7	0.04	0.1
O7.5 III	35.1	35.0	16.2	3.47	5.56	2500	−6.55	2.0×10^2		− 1.0 −		−6.0	70	28	0.3	0.1	1	0.2	0.04	0.1

& Owocki (2005) and Rubio-Díez et al. (2022). Consequently, we adopt a non-standard radially dependent volume filling factor $f(r)$ of the form

$$f(r) = f_\alpha + (1 - f_\alpha)\exp(-v(r)/f_\beta) + (f_\delta - f_\alpha)\exp([v(r) - v_\infty]/f_\gamma),$$

adopting $f_\alpha = 0.1$, $f_\beta = 200$ km s^{-1}, $f_\gamma = 100$ km s^{-1}, and $f_\delta = 0.5$ to ensure that the volume filling factor is ∼0.1 for the inner wind, and 0.5 in the extreme outer wind where the [O III] fine-structure line originates in γ Vel.

To investigate the physical conditions found in the [O III] 88.4 μm formation region of γ Vel, we computed a CMFGEN model atmosphere that extends to $4.5 \times 10^6 R_*$, i.e. spanning $-0.4 \leq \log(N_e/\text{cm}^{-3}) \leq 16.8$, requiring a significantly larger number of depth points (111) with respect to standard calculations (∼50) that extend to several hundred radii. The large outer boundary necessitates adiabatic cooling, with densities closely approximating those of the ambient ISM. In order to mitigate against vanishingly small populations of high ionization stages in the outer wind, we include X-rays. We consider the impact of f_δ on elemental abundances in Section. 4.1.

We have undertaken an analysis of the WC8 component of γ Vel, updated from De Marco et al. (2000) that was based on the He I λ5876, λ10830, He II λ4686, λ5411, and C III λ6727–73, C IV λ5411 diagnostics, but adjust our solution to the revised (higher) distance. The dereddened spectral energy distribution of γ Vel from *IUE*, *ISO* SWS+LWS and *Herschel* PACS is compared to the theoretical WC8+O model for our adopted light ratio in Fig. 3. The WC8+O model reproduces observations well up to ∼10 μm, but thereafter falls below spectrophotometric data.

Our spectroscopic luminosity, $\log L/L_\odot = 5.3$ infers a mass of ∼10.6 $M_\odot$ (Schaerer & Maeder 1992) somewhat higher than the dynamically determined value of 9.0 ± 0.6 $M_\odot$ from North et al. (2007), inferring $\log L/L_\odot = 5.18 \pm 0.05$. We support the previous determination of C/He = 0.15 by number, based on He II λ5411 and C IV λ5471, and consider the carbon-to-helium ratio to be relatively secure, i.e. $X_C = 30^{+3}_{-3}$ per cent. C/O = 5 by number was adopted by De Marco et al. (2000) since a determination of oxygen was not possible from weak/blended optical lines. Our revised physical and wind properties are derived based on the optical C III-IV diagnostics, primarily C III λ4647–51, 5696, 6727–73, 8500, plus C IV λ4441, 5471, 5801–12, 7724 plus He II λ4686. Low ionization lines including C II λλ6578–83, λλ7231–37 and He I λ5876 are somewhat underpredicted, as is He I λ1.083 μm with respect to NTT-EMMI spectroscopy of De Marco et al. (2000).

We present a comparison between our updated WC8 model and spectroscopic observations in Fig. 4, including the combined WC8+O7.5 III synthetic spectrum, using parameters for the O star companion updated from De Marco & Schmutz (1999) to reflect the revised distance. We include a comparison with λλ975-1275 *Copernicus* U2 spectroscopy from March 1977 in the Appendix (Fig. A1). In the UV, the overall spectral energy distribution is well reproduced – iron blanketing in the O star produces the broad dip between 1500 and 1700 Å. Some of the prominent lines in the UV are matched satisfactorily (e.g. Si IV λ1722) with respect to *Copernicus* and *IUE* spectroscopy, although others are poorly reproduced (C III] λ1909, C III λ2297) noting the complex orbital phase dependence of UV resonance lines (St.-Louis, Willis & Stevens 1993).

The predicted near-IR spectrum of γ Vel compares qualitatively well with published near-IR spectroscopy, including C III 0.97 μm, C IV 2.08 μm (Barnes, Lambert & Potter 1974; Aitken, Roche & Allen 1982). The synthetic spectrum provides a reasonable match to C IV lines within the 2.4–5 μm *ISO*-SWS range, although strong He II lines at 4.05 μm (10–8) and 4.65 μm (14–10) are underpre-

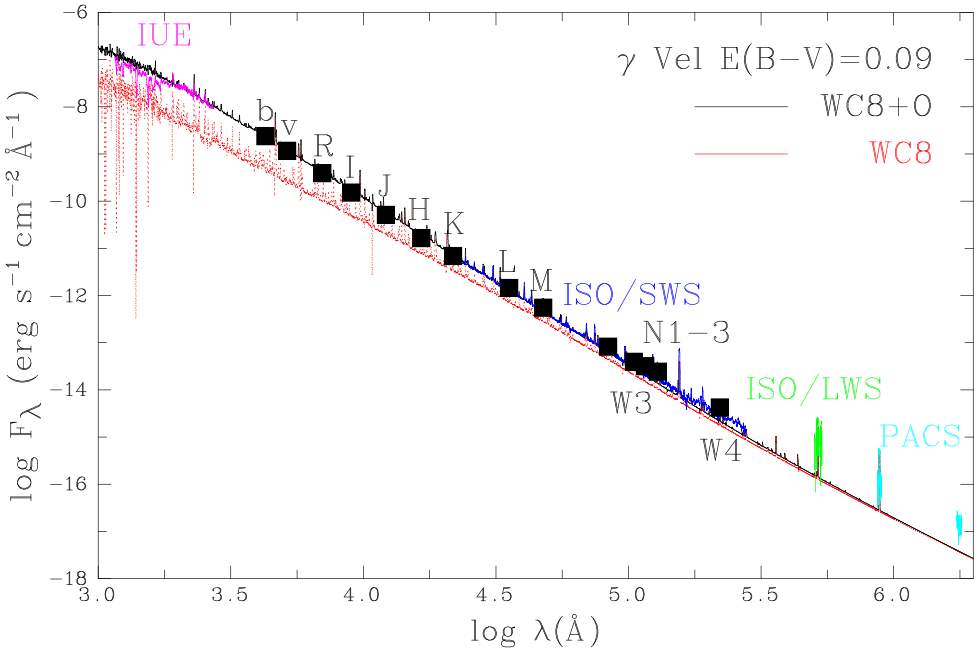

Figure 3. De-reddened spectral energy distribution of γ Vel from *IUE* (pink), *ISO* SWS (blue), and LWS ([O III] 52 μm region only, green) and *Herschel* PACS spectrophometry (cyan), together with combined theoretical WC8+O model (black) and WC8 (red) model, plus optical-IR photometry (Johnson et al. 1966; Williams et al. 1990; De Marco et al. 2000; Wright et al. 2010).

dicted. Beyond 5 μm, the overall emission line spectrum is rather too weak with respect to *ISO*-SWS observations, especially for He II 7.45 μm (6–5), C III 12.4 μm (14–13), and He II 19.4 μm (16–14). Overall, the C III–IV spectrum of γ Vel is reproduced significantly better than De Marco et al. (2000), albeit with He I less satisfactory.

We show the resulting wind properties as a function of electron density in Fig. 5. Optical emission lines form within the dense inner wind ($N_e \sim 10^{11-12}$ cm^{-3}), where the temperature is several 10^4 K (Hillier 1989; Hillier & Miller 1999). Strong metal line cooling leads to a relatively low wind temperature of $T_e = 7000$ K for intermediate densities ($N_e \sim 10^{6-8}$ cm^{-3}), corresponding to $\sim 10^{2.5} \leq r/R_* \leq 10^{3.5}$. In the extreme outer wind beyond $r \sim 10^5 R_*$ $N_e < 750$ cm^{-3}, and $T_e < 800$ K. Fig. 5 also shows the wind velocity and volume filling factor of this model, the latter corresponding to $f = 0.1$ for the optical lines and $f = 0.5$ for the IR fine-structure lines.

The density dependence of ionization for carbon, oxygen, neon, and sulphur, as predicted by this CMFGEN model for the WC8 star, is shown in Fig. 5. C^{2+}, O^{2+}, S^{+3+}, and Ne^{2+} are predicted to be the dominant ionization stages of carbon, oxygen, sulphur, and neon in the outer wind at $N_e \sim 10^5$ cm^{-3}, corresponding to the fine-structure line-forming regions of neon and sulphur, with O^{2+} predicted to remain the dominant ion of oxygen in the extreme outer wind, where [O III] fine-structure lines originate, as illustrated in Fig. 6. Additional elements are presented in the Appendix (Fig. B1). He^+ remains the dominant ion of helium for all densities below $N_e \sim 10^{11.5}$ cm^{-3}, while the dominant ions of argon and calcium in the outer wind are Ar^{3+} and Ca^{3+}, with iron transitioning from Fe^{4+} to Fe^{3+} at $N_e \sim 10^{4.5}$ cm^{-3}.

Fig. 7 reveals satisfactory fits to [S IV] 10.5 μm and [O III] 88.4 μm for mass fractions of 0.04 per cent and 1.0 per cent, respectively, plus both [Ne II] 12.8 μm and [Ne III] 15.5 μm for an adopted mass fraction of 1.7 per cent. Consequently, we can be confident with the inferred oxygen, neon, and sulphur abundances (for our adopted wind clumping). [Ne II], [Ne III], and [O III] fine-structure lines show central subpeaks together with additional peaks at ± 1000 km s^{-1}. This structure contrasts with flat topped predictions from CMFGEN in Fig. 7.

The origin for this structure may be linked with the binary nature of γ Vel, specifically the colliding wind region between the WC8 and O star components. The wind momentum of the WC8 component exceeds the O star by a factor of ∼30, so the O star wind will be strongly confined. Nevertheless the post-shock region of the colliding winds may contribute to the observed emission. Recent *JWST* MIRI imaging of the long period WC7+O binary system WR 140 reveal nested rings of dust emission (Lau et al. 2022), suggesting that a relic of its colliding winds persist to large radii. Curiously, subpeak structure is not apparent for [S IV] in γ Vel, but would be expected from its overlapping line formation region to [Ne II–III] (recall Fig. 6). Subpeaks are observed in [O III] for other binary and *single* WC stars (Crowther, private communication), so the origin of sub-peak structures remains uncertain.

Fig. 8 compares three synthetic WC8 models in the UV, visual, and far-IR with O/He = 0.002, 0.004, and 0.006 by number. These illustrate the clear correlation between oxygen abundance and [O III] 52 μm, 88 μm strength in contrast to the few oxygen lines in the UV/optical. We will revisit our inferred abundances in Section 4, but favour an oxygen abundance of ∼1 per cent by mass for γ Vel from our CMFGEN analysis, which is compared to evolutionary predictions in Section 5.

4 γ VEL ABUNDANCES FROM FINE-STRUCTURE LINES

4.1 Oxygen

We are able to independently calculate the fractional ionic abundance of O^{2+} from the [O III] 88.36 μm fine-structure line following the approach of Barlow, Roche & Aitken (1988), modified by Dessart et al. (2000) to incorporate wind clumping. This method was

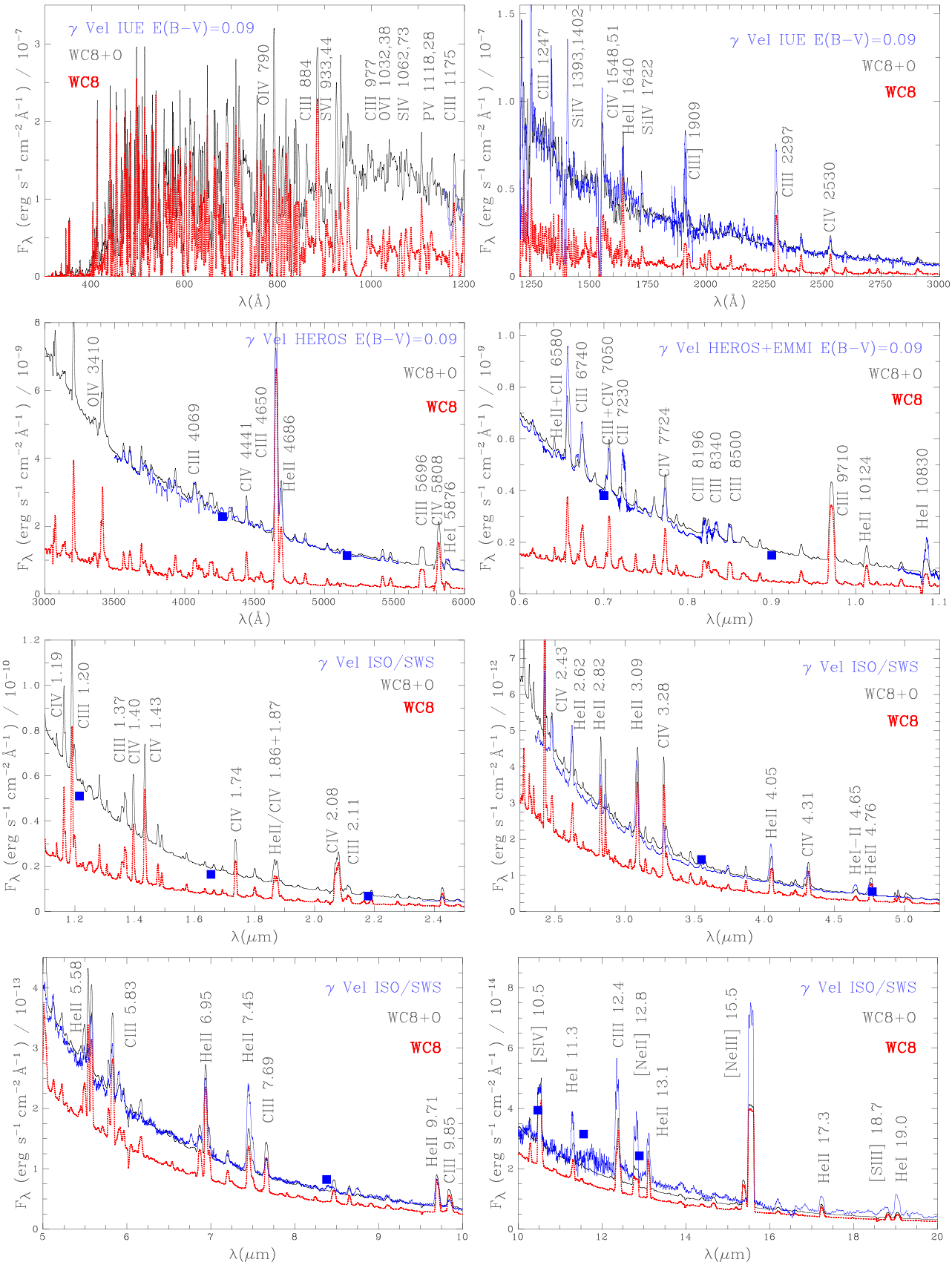

Figure 4. De-reddened UV *IUE/HIRES* spectroscopy (phase 0.5), calibrated optical ESO 50cm+HEROS and NTT+EMMI He I λ10830 spectroscopy, *ISO* SWS infrared spectroscopy of γ Vel (blue), together with theoretical WC8+O model (black) and WC8 component (red), excluding correction for interstellar H I. Optical-IR photometry (Johnson et al. 1966; Williams et al. 1990; De Marco et al. 2000; Wright et al. 2010) is presented as blue boxes.

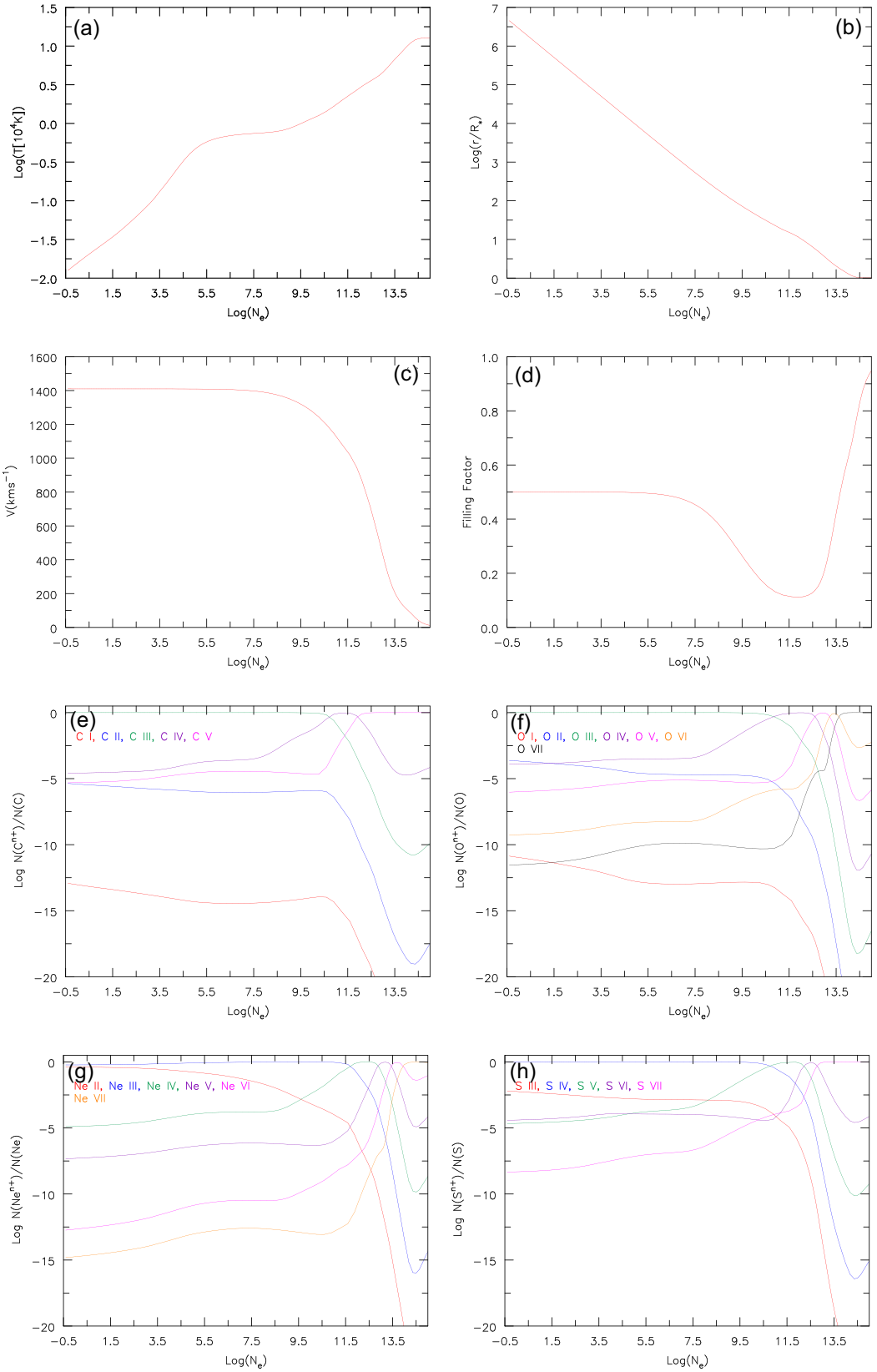

Figure 5. WC8 wind structure for $\log N_e$ (cm^{-3}) versus (a) $\log T_e$ (10^4 K, red); (b) $\log r/R_*$ (red); (c) velocity $v(r)$ (km s^{-1}, red); (d) clumping volume filling factor f (red); ionization structure of (e) carbon: log C^0/C (red), C^+/C (blue), C^{2+}/C (green), C^{3+}/C (purple), C^{4+}/C (pink); (f) oxygen: log O^0/O (red), O^+/O (blue), O^{2+}/O (green), O^{3+}/O (purple), O^{4+}/O (pink), O^{5+}/O (orange), O^{6+}/O (black); (g) neon: log Ne^+/Ne (red), Ne^{2+}/Ne (blue), Ne^{3+}/Ne (green), Ne^{4+}/Ne (purple), Ne^{5+}/Ne (pink), Ne^{6+}/Ne (orange); (h) sulphur: log S^{2+}/S (red), S^{3+}/S (blue), S^{4+}/S (green), S^{5+}/S (purple), S^{6+}/S (pink). Higher ionization stages will dominate optically thick regions at high densities ($\log N_e \geq 13.5$).

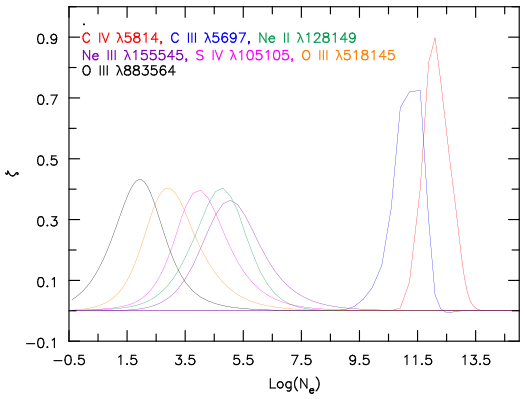

Figure 6. Line formation regions of selected spectral lines in the WC8 stellar wind of γ Vel: C IV λ5812 (red), C III λ5696 (blue) in the dense inner wind, [Ne II] 12.8 μm (green), [Ne III] 15.5 μm (purple), [S IV] 10.5 μm (pink) in the low density outer wind, plus [O III] 51.8 μm (orange) and 88.4 μm (black) in the very low density extreme outer wind.

originally devised to measure ionic neon abundances in γ Vel, and involves the [O III] line flux (from Section 2) and adopted wind properties (informed from Section 3).

The following abundance determination is applicable to an emission line formed by electronic transition between two fine-structure energy levels (u and l), occurring in the asymptotic region of a clumpy stellar wind, where material is on average flowing at a velocity v_∞ following a r^{-2} density distribution. If a flux I_{ul} is observed in the fine-structure line of a star residing at a distance d, the total power emitted by the star in this line is

$$4\pi d^2 I_{ul} = \int_0^\infty n_u A_{ul} h\nu_{ul} 4\pi r^2 f_{\rm clump}\, {\rm d}r \quad {\rm erg\,s^{-1}}, \tag{1}$$

where $h\nu_{ul}$ is the energy of a transition with probability A_{ul} (s^{-1}) of occurrence, n_u is the density of ions in the upper level, and $f_{\rm clump}$ is the volume filling factor in the [O III] line-forming region. The incorporation of this clumping factor is a modification to the original method of Barlow, Roche & Aitken (1988).

The density of ions in the upper level can alternatively be expressed as

$$n_u = f_u n_i \quad {\rm cm^{-3}}, \tag{2}$$

where n_i is the species ion density, of which a fraction f_u is in the upper level. Following Dessart et al. (2000), we use values of f_u calculated by solving the equations of statistical equilibrium for the O^{2+} ion, using the EQUIB code (Howarth et al. 2016), at 13 electron densities over the range $N_{\rm e} = 10^0$–10^{12} cm^{-3}, and electron temperatures $T_{\rm e} = 1000$–$10\,000$ K, for the collisional and radiative atomic data presented in Table 2.

Knowledge of the mass-loss rate and terminal wind speed become important when determining n_i. These properties are combined in the mass-loss parameter A (Barlow, Roche & Aitken 1988, equation 8) so that

$$n_u = \frac{f_u \gamma_i A}{f_{\rm clump} r^2} \quad {\rm cm^{-3}}, \tag{3}$$

where γ_i is the fraction of *all* ions that are species i (i.e. $\gamma(O^{2+})$, the desired result). Combining equations (1) and (3), the filling factor cancels and we are left with

$$I_{ul} = \frac{\gamma_i}{d^2} A_{ul} h\nu_{ul} A \int_0^\infty f_u(r,\, f_{\rm clump},\, T_e)\, {\rm d}r \quad {\rm erg\,s^{-1}cm^{-2}}. \tag{4}$$

At this point, we follow Dessart et al. (2000) by integrating over electron density, $N_{\rm e}$, removing the dependence of f_u on A (and hence $\dot{M}$) and filling factor.

Converting the integral in equation (4) to one over $N_{\rm e}$ and rearranging for the fractional ionic abundance, one obtains

$$\gamma_i = \frac{(4\pi\mu m_H v_\infty)^{1.5}}{ln(10)} \left(\frac{\sqrt{f_{\rm clump}}}{\dot{M}^{1.5}}\right) \frac{1}{F_u(N_e, T_e)} \frac{2d^2 I_{ul}}{\sqrt{\gamma_e} A_{ul} h\nu_{ul}}, \tag{5}$$

where

$$F_u(N_e, T_e) = \int_0^\infty \frac{f_u(N_e, T_e)}{\sqrt{N_e}}\, {\rm d}\log(N_e). \tag{6}$$

Equation (5) is ultimately what we use to calculate $\gamma(O^{2+})$ which is presented in Table 3, with the relevant atomic data used for their calculation given in Table 2, adopting $T_{\rm e} = 1000$ K. $\gamma(O^{2+}) = 3.3^{+0.7}_{-1.0} \times 10^{-3}$, corresponds to $O^{2+}/{\rm He} = 3.8^{+0.9}_{-1.1} \times 10^{-3}$ or $X_{\rm O} = 1.0^{+0.2}_{-0.3}$ per cent by mass, assuming O^{2+} is the dominant ion in the line-forming region of [O III] 88.36 μm (∼500 cm^{-3}).

The primary parameter affecting $\gamma(O^{2+})$ in γ Vel is wind clumping, which as discussed in Section 3, is assumed to persist in the extreme outer winds of WC stars with a volume filling factor $f_{\rm out} = 0.5 \pm 0.25$. To quantify the effect of this uncertainty, we evaluate $\gamma(O^{2+})$ at the extremes of this range, with mass-loss rates fixed at the values derived using $f_{\rm in} = 0.1$.

An alternative O^{2+} line is available, namely [O III] 51.81 μm from *ISO*-LWS (Fig. 2). This line has a critical density an order of magnitude higher than [O III] 88.4 μm (recall Table 2) as illustrated in Fig. 6. If the ionic state of oxygen were to substantially change in the extreme outer wind one would derive different values of $\gamma(O^{2+})$ using [O III] 88.36 μm and [O III] 51.81 μm, even though this is not predicted from our CMFGEN model (Fig. 5). We derive $\gamma(O^{2+}) = 4.1^{+0.9}_{-1.2} \times 10^{-3}$ from [O III] 51.81 μm. This corresponds to $O^{2+}/{\rm He} = 4.7^{+1.1}_{-1.4} \times 10^{-3}$ or $X_{\rm O} = 1.3^{+0.2}_{-0.4}$ per cent by mass, and is in reasonable agreement with that obtained from the *Herschel* PACS observations (Table 3), despite the low quality of the *ISO*/LWS spectroscopy.

Fine-structure lines of different ionization stages of the same atomic species provide the best probes of ionization structure. Unfortunately, the ground state configuration of O^+ does not provide a suitable transition, whereas the extent of O^{3+} may be probed using [O IV] 25.89 μm ($^2P^\circ_{1/2}$–$^2P^\circ_{3/2}$). This line has a critical density of $N_{\rm crit} \sim 10^4$ cm^{-3}, so would be formed interior to both [O III] lines considered thus far. This line is *not* detected in *ISO* SWS spectroscopy of γ Vel (van der Hucht et al. 1996), or indeed *Spitzer* IRS scans of other late WC stars (Crowther, priv comm), suggesting that O^{3+} contributes negligibly to the outer wind of γ Vel. Overall, fine-structure lines of oxygen support the predicted outer wind structure of γ Vel presented in Fig. 5.

4.2 Neon and sulphur

We now consider fine-structure lines of other elements, namely neon ([Ne II] 12.8 μm, [Ne III] 15.5 μm) and sulphur ([S IV] 10.5 μm) from *ISO*-SWS (van der Hucht et al. 1996; Dessart et al. 2000). [S III] 18.7 μm is blended with C III 18.8 μm (16–15) and He I 18.6 μm (3d ^{3}D - ^{3}P°) so its detection is tentative. [Ne III] 36.0 μm lies in the low sensitivity band 4 of *ISO*'s SWS instrument (de Graauw et al. 1996), so is not measurable. One would expect $I_{36.0}/I_{15.5} \sim 0.04$ at $T_{\rm e} = 5000$ K and $N_{\rm e} = 10^5$ cm^{-3} from EQUIB (Howarth et al. 2016), i.e. $I_{36.0} \sim 3.5 \times 10^{-12}$ erg s^{-1} cm^{-2}. There is no evidence for either [Ar II] 6.98 μm or [Ar III] 8.99 μm in *ISO*-SWS spectroscopy

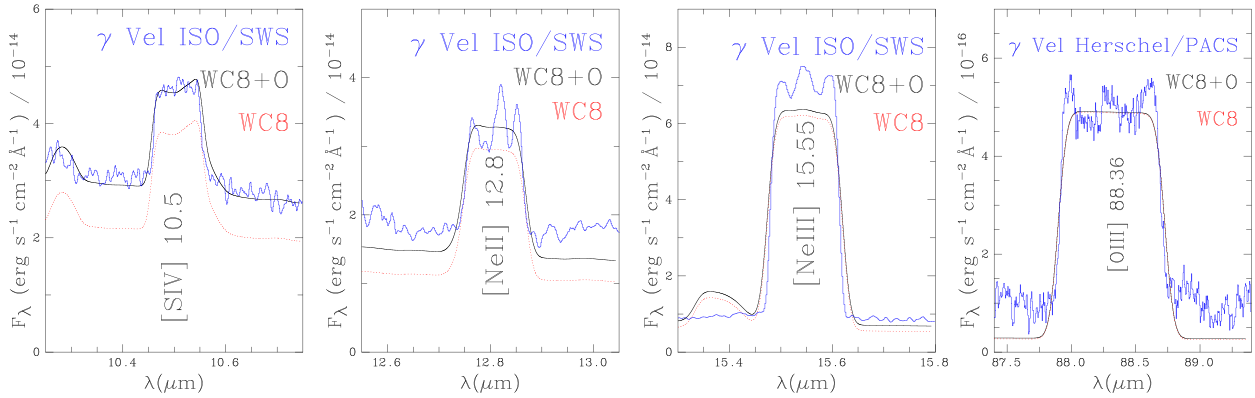

Figure 7. γ Vel's primary mid-IR fine-structure lines [S IV] 10.51 μm (*ISO*/SWS), [Ne II] 12.81 μm (*ISO*/SWS), [Ne III] 15.55 μm (*ISO*/SWS), [O III] 88.36 μm (*Herschel*/PACS), shown in blue, together with the theoretical WCI+O model (black) and WC8 component (red), adjusted for instrumental broadening (R = 1700, 1200, 1500, 2500, respectively).

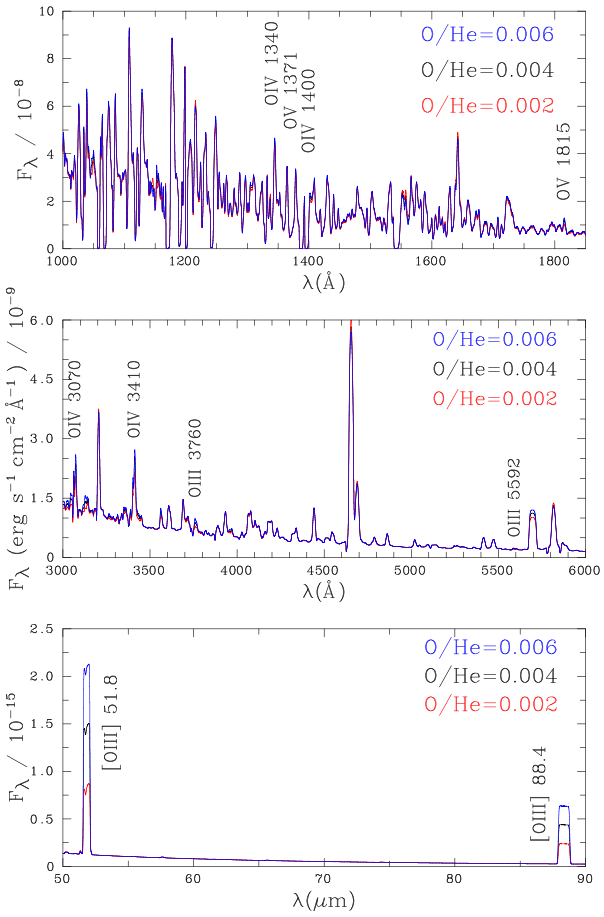

Figure 8. Synthetic UV (top), visual (centre), far-IR (bottom) WC8 spectra for O/He=0.002 (X_O = 0.5 per cent, red), 0.004 (X_O = 1.1 per cent, black), and 0.006 (X_O = 1.6 per cent, blue) highlighting the sensitivity of fine-structure lines of [O III] to oxygen abundance. UV/optical lines are relatively insensitive to a factor of three difference in oxygen content owing to the dominant helium-carbon line spectrum.

of γ Vel, as expected from the predicted CMFGEN ionization balance structure of argon which suggests Ar^{3+} is the dominant ion in the outer wind (Fig. B1). Ignace et al. (2001) discuss [Ca IV] 3.21 μm for a sample of WR stars including γ Vel. However, it is clear that

Table 2. Atomic data for [O III] 88.36 μm and 51.81 μm fine-structure lines, drawn from Nussbaumer & Storey (1981) and Storey, Sochi & Badnell (2014) for radiative and collisional rates, respectively, with critical densities N_{crit} from Rubin (1989).

Transition $u-l$	λ μm	ω_u	ω_l	A_{ul} (s^{-1})	Ω_{ul} 1 000K	$\log(N_{crit}/cm^{-3})$ 8000 K
$^3P_2 - {}^3P_1$	51.814	5	3	9.76×10^{-5}	1.12	3.5
$^3P_1 - {}^3P_0$	88.356	3	1	2.62×10^{-5}	0.52	2.7

Table 3. Fine-structure line fluxes and inferred ionic abundances for γ Vel using the integral method and a uniform filling factor of $f = 0.5 \pm 0.25$. Atomic data for the transitions are given in Table 2 or Dessart et al. (2000), aside from updated collision strengths for [S IV] (Tayal 2000) and [Ne III] (McLaughlin & Bell 2000).

λ μm	ID	Flux 10^{-12} (erg s^{-1} cm^{-2})	Instrument	Ref	T_e (K)	γ_i 10^{-4}	X_i/He 10^{-4}
10.5	[S IV]	15 ± 1	*ISO* SWS	a	2000	$0.6^{+0.2}_{-0.2}$	$0.7^{+0.2}_{-0.2}$
12.8	[Ne II]	18 ± 1	*ISO* SWS	a	5000	10^{+2}_{-3}	12^{+2}_{-4}
15.5	[Ne III]	82 ± 1	*ISO* SWS	a	5000	41^{+9}_{-12}	47^{+11}_{-14}
51.8	[O III]	8 ± 1	*ISO* LWS	b	1000	41^{+9}_{-12}	47^{+11}_{-14}
88.4	[O III]	3.4 ± 0.5	*Herschel* PACS	b	1000	33^{+7}_{-10}	38^{+9}_{-11}

Note. a: Dessart et al. (2000); b: this work.

C III 3.20 μm (14–11) dominates the observed feature (their fig. 1) in the case of γ Vel.

Using the method introduced above, together with atomic data from Dessart et al. (2000, their table 9), we use these S and Ne line flux measurements to reassess the fractional abundances of the respective ionic species in γ Vel. These are included in Table 3 and provide an independent insight into the empirical ionization balance in the outer wind versus predictions (Fig. 6) in which [Ne II] 12.8 μm and [Ne III] 15.5 μm form at $\log(N_e/cm^{-3}) = 5 \pm 1 (T_e \sim 5000$ K) and [S IV] 10.5 μm forms at $\log(N_e/cm^{-3}) = 4 \pm 1 (T_e \sim 2000$ K).

For neon, the dominant fine-structure line is [Ne III] 15.5 μm, from which $Ne^{2+}/He = 4.7^{+1.1}_{-1.4} \times 10^{-3}$ or $X_{Ne^{2+}} = 1.6^{+0.3}_{-0.5}$ per cent by mass ($T_e \sim 5000$ K is adopted), consistent with expectations for the products of the CNO cycle being converted to ^{22}Ne. A neon abundance 25 per cent larger is obtained by including Ne^+ from [Ne II] 12.8 μm, corresponding to $X_{Ne} = 2.0^{+0.4}_{-0.6}$ per cent, in close agreement with our CMFGEN modelling result of $X_{Ne} = 1.7$ per cent.

Table 4. Comparison between physical and wind properties of the WC8 component of γ Vel determined here adopting the (far) interferometric distance (North et al. 2007) and those from De Marco et al. (2000) using the original (near) *Hipparcos* distance of Schaerer, Schmutz & Grenon (1997). A volume filling factor of 0.1 for the inner wind volume filling factor is adopted in both cases. Our preferred oxygen abundance is based on *Herschel* PACS spectroscopy of [O III] 88 μm.

Study	De Marco et al.		This work	
Distance (pc)	258^{+41}_{-31}		336^{+8}_{-7}	
T_*/kK	57		90	
log L/L$_\odot$	5.0		5.31	
$R_*/R_\odot$	3.2		1.9	
log $\dot{M}/M_\odot$yr^{-1}	–5.0		–4.84	
v_∞ (km s^{-1})	1550		1500 ± 20	
Q_0 (ph s^{-1})	48.81		49.09	
Q_1 (ph s^{-1})	47.76		48.12	
C/He (X_C)	0.15	(28 per cent)	0.15 ± 0.02	(30 ± 3 per cent)
O/He (X_O)	0.03[a]	(8 per cent[a])	$0.0038^{+0.0009}_{-0.0011}$	($1.0^{+0.2}_{-0.3}$ per cent)
Ne/He (X_{Ne})	‡0.003	(‡1 per cent)	$0.0059^{+0.0013}_{-0.0017}$	($2.0^{+0.4}_{-0.6}$ per cent)
S/He (X_S)	‡6×10^{-5}	(‡0.03 per cent)	$7 \pm 2 \times 10^{-5}$	(0.04 ± 0.01 per cent)

Note. [a]O/C=0.2 by number adopted; ‡: Dessart et al. (2000).

Recall from Fig. 5 that Ne$^+$ is (narrowly) the secondary ion of neon within its outer wind.

The inferred sulphur abundance is S/He $= 0.7^{+0.2}_{-0.2} \times 10^{-4}$ by number or $X_S \sim 0.04 \pm 0.01$ per cent from [S IV] 10.5 μm, in good agreement with the CMFGEN modelling ($T_e \sim 2000$ K is adopted for its line-forming region). Our value is in close agreement with the solar value of log (S/H) + 12 = 7.16 ± 0.11 (Magg et al. 2022), which equates to $X_S = 0.046^{+0.014}_{-0.010}$ per cent by mass, as expected for an unprocessed element. In principle it could be somewhat higher if there is a non-negligible contribution from S^{2+}. Fig. 5 includes the predicted ionization structure of the WC8 outer wind of sulphur, revealing that the dominant ionization stage of sulphur is predicted to be S^{3+}, so one would expect [S IV] 10.5 μm to be dominant over [S III] 18.7 μm, as is observed.

5 DISCUSSION AND CONCLUSIONS

γ Vel is a well-known binary system, with a period of 78.5 d (Niemela & Sahade 1980) and eccentricity of 0.33 (North et al. 2007), from which component masses of 28.5 ± 1.1 M$_\odot$ (O7.5 III) and 9.0 ± 0.6 M$_\odot$ (WC8) have been established.

Binary interaction is capable of drastically altering the evolution of a massive star via mass and angular momentum exchange. It is likely that the WC8 component of γ Vel has undergone Case B mass-transfer with its O-star companion (Eldridge 2009), indicating a deviation from single-star evolution. We compare our physical and wind properties of the WC8 component of γ Vel with previous results of De Marco et al. (2000) inTable 4. Revised values follow from a combination of the modern interferometric distance to γ Vel, improved treatment of line blanketing – De Marco et al. (2000) solely considered Ca and Fe amongst intermediate and heavy elements – and the availability of fine-structure observations of oxygen courtesy of *Herschel*.

We have directly measured the oxygen abundance within the wind of γ Vel from far-IR fine-structure lines of [O III] using two complementary approaches, detailed spectroscopic analysis with the CMFGEN model atmosphere code ($X_O \sim 1.1$ per cent), and following the analytic method devised by Barlow, Roche & Aitken (1988) and updated by Dessart et al. (2000) ($X_O \sim 1.0 \pm 0.3$ per cent),

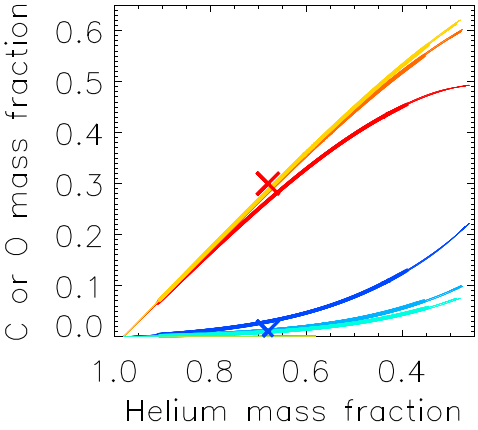

Figure 9. Observed abundances by mass of carbon (red cross) and oxygen (blue cross) versus helium for γ Vel plus predictions from BPASS v2.4 (Eldridge et al. 2017) for $M_{1,init} = 35$–40 M$_\odot$, $q = 0.5$–0.9, log P_{init}/d =1–2 with ^{12}C(α, γ)^{16}O reaction rates from Angulo et al. (1999, red + blue), Kunz et al. (2002, red + pale blue) and Kunz et al. (2002, orange + cyan) scaled by 0.75.

Oxygen is overwhelmingly in the form of O^{2+} in the outer wind of γ Vel. Uncertain nuclear burning rates may be constrained by these quantities, as the balance between carbon and oxygen in massive stars is solely determined by the competition of $3\alpha \rightarrow {}^{12}$C and ^{12}C($\alpha$, γ)^{16}O processes, the latter of which remains uncertain (Buchmann & Barnes 2006).

The importance of the ^{12}C(α, γ)^{16}O reaction rate in determining nucleosynthetic yields has been investigated by Imbriani et al. (2001), who model the evolution a 25 M$_\odot$ star using historical cross-sections for this reaction (Caughlan et al. 1985; Caughlan & Fowler 1988). They find that a doubling of the reaction rate in this case halves the carbon mass fraction at the end of helium burning, corresponding to a higher O/C ratio in the star as a whole. These authors conclude that the higher of their two considered ^{12}C(α, γ)^{16}O reaction rates provides better agreement with the solar abundance pattern, in agreement with the earlier work of Weaver & Woosley (1993). It is these studies that have motivated the choice of reaction rates used in many contemporary models of stellar evolution.

However, this preference for a higher reaction rate is at odds with the oxygen abundances presented here. A similar issue has been noted by Aadland et al. (2022) for LMC WO stars. They provided predictions from the Geneva evolutionary model based on the NACRE reaction rates and NACRE rates divided by a factor of 3 (their fig. 18), which suppress the production of oxygen with respect to carbon. Aadland et al. (2022) also present BPASS models using Kunz et al. (2002) rates plus these rates scaled by 0.75, quantitatively in better agreement with our results.

In Fig. 9, we show C and O mass fractions versus He for BPASS v2.4 binary evolution models (Eldridge et al. 2017) tailored for γ Vel. These involve a 35–40 M$_\odot$ primary, $q = 0.5$–0.9, and log (P_{init}/d) = 1–2 at solar metallicity (Eldridge 2009). ^{12}C(α, γ)^{16}O reaction rates are from NACRE (Angulo et al. 1999), Kunz et al. (2002) and the latter scaled by 0.75 (Aadland et al. 2022). Table 5 provides a summary of predictions for different reaction rates for a 35 M$_\odot$ primary once $X_C/X_{He} = 0.45$ (by mass) at the stellar surface. The dynamical mass of the WC8 component from North et al. (2007) is well matched for this combination of initial parameters. Our spectroscopic luminosity is a little higher, favouring a slightly higher initial (current) mass, implying a lower system age (∼5 Myr).

Table 5. Comparison between observed (bold) and predicted BPASS (Eldridge et al. 2017) v2.4 properties for γ Vel binary for $M_{1,\rm init} = 35$ M$_\odot$, $q = 0.8$, log ($P_{\rm init}$/d) = 1.5 (Eldridge 2009) once $X_{\rm C}/X_{\rm He} = 0.45$ at the surface.

τ (Myr)	M_1 (M$_\odot$)	log L_1 (L$_\odot$)	$X_{\rm He}$ (per cent)	$X_{\rm C}$ (per cent)	$X_{\rm O}$ (per cent)	$X_{\rm Ne}$ (per cent)	^{12}C(α, γ)^{16}O rates
5.58	9.1	5.21	64.9	29.2	3.5	1.9	Angulo et al. (1999)
5.57	9.2	5.23	66.4	29.9	1.3	1.9	Kunz et al. (2002)
5.57	9.2	5.23	66.6	30.0	1.0	1.9	Kunz et al. (2002) × 0.75
...	...	**5.31**	$\mathbf{67}^{+2}_{-2}$	$\mathbf{30}^{+3}_{-3}$	$\mathbf{1.0}^{+0.3}_{-0.3}$	$\mathbf{2.0}^{+0.4}_{-0.6}$	

From Fig. 9 and Table 5 it is apparent that either the standard or scaled Kunz et al. (2002) reaction rates are favoured by our results for γ Vel, although it is not possible to exclude modest revisions in view of uncertainties in volume filling factors. Predicted neon abundances are also in excellent agreement with our empirical results from mid-IR fine-structure lines ($X_{\rm Ne} = 2.0^{+0.4}_{-0.6}$ per cent), as anticipated for CNO nuclei processed into ^{14}N during H burning, subsequently converted to ^{22}Ne via the ^{14}N(α, γ)^{18}F($e^+\nu$)^{18}O(α, γ)^{22}Ne reaction. The inferred sulphur abundance from mid-IR fine-structure diagnostics ($X_{\rm S} = 0.04 \pm 0.01$ per cent) is in excellent agreement with the solar value (Magg et al. 2022).

In conclusion, we have presented successful modelling of IR fine-structure lines of γ Vel with CMFGEN, together with the complementary approach of Barlow, Roche & Aitken (1988) and Dessart et al. (2000), suggesting oxygen and neon determinations from similar analyses of other WC (and WO) stars is realistic based on archival *Herschel*-PACS and *Spitzer*-IRAC spectroscopy, plus potentially *JWST*-MIRI spectroscopy of sources too faint for previous IR missions.

ACKNOWLEDGEMENTS

Thanks to Chris Rosslowe who performed initial measurements of *Herschel* PACS spectroscopy of WC and WO stars. Thanks to Jan J Eldridge for providing bespoke Binary Population and Spectral Synthesis (BPASS) models (v2.4) appropriate for γ Vel. See Eldridge et al. (2017, v2.1), Stanway & Eldridge (2018, v2.2), and Byrne et al. (2022, v2.3) for a description of previous BPASS versions. Thanks to Alex Fullerton for converting archival *Copernicus* spectroscopy of γ Vel into a user friendly format. Comments from the anonymous referee helped to improve the manuscript. PAC and JMB are supported by the Science and Technology Facilities Council research grant ST/V000853/1 (PI. V. Dhillon). JDH acknowledges support from STScI theory grant HST-AR-16131.001-A. PR thanks the European Space Agency (ESA) and the Belgian Federal Science Policy Office (BELSPO) or their support in the framework of the PRODEX Programme.

DATA AVAILABILITY

The *Herschel* PACS spectrum will be provided on request, while the CMFGEN model of the WC8 star will be made available at https://sites.pitt.edu/ hillier/web/CMFGEN.htm.

REFERENCES

Aadland E., Massey P., Hillier D. J., Morrell N. I., Neugent K. F., Eldridge J. J., 2022, ApJ, 931, 157
Aitken D. K., Roche P. F., Allen D. A., 1982, MNRAS, 200, 69P
Aller L. H., Faulkner D. J., 1964, ApJ, 140, 167
Angulo C. et al., 1999, Nucl. Phys. A, 656, 3
Baade D., Schmutz W., van Kerkwijk M., 1990, A&A, 240, 105
Barlow M. J., Roche P. F., Aitken D. K., 1988, MNRAS, 232, 821
Barnes T. G., Lambert D. L., Potter A. E., 1974, ApJ, 187, 73
Bohlin R. C., 1975, ApJ, 200, 402
Brinchmann J., Kunth D., Durret F., 2008, A&A, 485, 657
Buchmann L. R., Barnes C. A., 2006, Nucl. Phys. A, 777, 254
Byrne C. M., Stanway E. R., Eldridge J. J., McSwiney L., Townsend O. T., 2022, MNRAS, 512, 5329
Caughlan G. R., Fowler W. A., 1988, At. Data Nucl. Data Tables, 40, 283
Caughlan G. R., Fowler W. A., Harris M. J., Zimmerman B. A., 1985, At. Data Nucl. Data Tables, 32, 197
Chapman J. M., Leitherer C., Koribalski B., Bouter R., Storey M., 1999, ApJ, 518, 890
Clegg P. E. et al., 1996, A&A, 315, L38
Crowther P. A., 2007, ARA&A, 45, 177
Crowther P. A., Dessart L., Hillier D. J., Abbott J. B., Fullerton A. W., 2002, A&A, 392, 653
Crowther P. A., Hadfield L. J., Clark J. S., Negueruela I., Vacca W. D., 2006, MNRAS, 372, 1407
de Graauw T. et al., 1996, A&A, 315, L49
De Marco O., Schmutz W., 1999, A&A, 345, 163
De Marco O., Schmutz W., Crowther P. A., Hillier D. J., Dessart L., de Koter A., Schweickhardt J., 2000, A&A, 358, 187
de Mink S. E., Langer N., Izzard R. G., Sana H., de Koter A., 2013, ApJ, 764, 166
de Zeeuw P. T., Hoogerwerf R., de Bruijne J. H. J., Brown A. G. A., Blaauw A., 1999, AJ, 117, 354
Dessart L., Crowther P. A., Hillier D. J., Willis A. J., Morris P. W., van der Hucht K. A., 2000, MNRAS, 315, 407
Eenens P. R. J., Williams P. M., 1994, MNRAS, 269, 1082
Eldridge J. J., 2009, MNRAS, 400, L20
Eldridge J. J., Stanway E. R., Xiao L., McClelland L. A. S., Taylor G., Ng M., Greis S. M. L., Bray J. C., 2017, Publ. Astron. Soc. Aust., 34, e058
Esteban C., Vilchez J. M., Smith L. J., Clegg R. E. S., 1992, A&A, 259, 629
Fowler W. A., 1984, Science, 226, 922
Franciosini E., Sacco G. G., Jeffries R. D., Damiani F., Roccatagliata V., Fedele D., Randich S., 2018, A&A, 616, L12
Fynbo H. O. U. et al., 2005, Nature, 433, 136
García-Lario P., 2000, in Salama A., Kessler M. F., Leech K., Schulz B., eds, ESA SP-456: ISO Beyond the Peaks: The 2nd ISO Workshop on Analytical Spectroscopy. ESA, Noordwijk, p. 267
Gräfener G., Koesterke L., Hamann W.-R., 2002, A&A, 387, 244
Hillier D. J., 1989, ApJ, 347, 392
Hillier D. J., 1991, A&A, 247, 455
Hillier D. J., Miller D. L., 1998, ApJ, 496, 407
Hillier D. J., Miller D. L., 1999, ApJ, 519, 354
Howarth I. D., Murray J., Mills D., Berry D. S., 2004, Starlink User Note 50, Council for the Central Laboratory of the Research Councils
Howarth I. D., Adams S., Clegg R. E. S., Ruffle D. P., Liu X. W., Pritchet C. J., Ercolano B., 2016, Astrophysics Source Code Library, record ascl:1603.005
Ignace R., Cassinelli J. P., Quigley M., Babler B., 2001, ApJ, 558, 771
Imbriani G., Limongi M., Gialanella L., Terrasi F., Straniero O., Chieffi A., 2001, ApJ, 558, 903
Jeffries R. D., Naylor T., Walter F. M., Pozzo M. P., Devey C. R., 2009, MNRAS, 393, 538
Jeffries R. D. et al., 2017, MNRAS, 464, 1456
Johnson H. M., 1978, ApJS, 36, 217
Johnson H. L., Mitchell R. I., Iriarte B., Wisniewski W. Z., 1966, Commun. Lunar Planet. Lab., 4, 99
Kunz R., Fey M., Jaeger M., Mayer A., Hammer J. W., Staudt G., Harissopulos S., Paradellis T., 2002, ApJ, 567, 643
Kurosawa R., Hillier D. J., Pittard J. M., 2002, A&A, 388, 957
Lau R. M. et al., 2022, Nat. Astron., 6, 1308
López-Sánchez Á. R., Esteban C., 2010, A&A, 517, A85

McLaughlin B. M., Bell K. L., 2000, J. Phys. B: At. Mol. Phys., 33, 597
Magg E. et al., 2022, A&A, 661, A140
Meynet G., Maeder A., 2005, A&A, 429, 581
Morris P. W., van der Hucht K. A., Crowther P. A., Hillier D. J., Dessart L., Williams P. M., Willis A. J., 2000, A&A, 353, 624
Morris P. W., Crowther P. A., Houck J. R., 2004, ApJS, 154, 413
Najarro F., Hanson M. M., Puls J., 2011, A&A, 535, A32
Niemela V. S., Sahade J., 1980, ApJ, 238, 244
North J. R., Tuthill P. G., Tango W. J., Davis J., 2007, MNRAS, 377, 415
Nussbaumer H., Storey P. J., 1981, A&A, 99, 177
Osterbrock D. E., Ferland G. J., 2006, Astrophysics of Gaseous Nebulae and Active Galactic Nuclei. University Science Books, Sausilito, CA
Owocki S. P., Rybicki G. B., 1984, ApJ, 284, 337
Poglitsch A. et al., 2010, A&A, 518, L2
Prinja R. K., Barlow M. J., Howarth I. D., 1990, ApJ, 361, 607
Puls J., Markova N., Scuderi S., Stanghellini C., Taranova O. G., Burnley A. W., Howarth I. D., 2006, A&A, 454, 625
Rate G., Crowther P. A., 2020, MNRAS, 493, 1512
Roche P. F., Colling M. D., Barlow M. J., 2012, MNRAS, 427, 581
Rubin R. H., 1989, ApJS, 69, 897
Rubio-Díez M. M., Sundqvist J. O., Najarro F., Traficante A., Puls J., Calzoletti L., Figer D., 2022, A&A, 658, A61
Runacres M. C., Owocki S. P., 2002, A&A, 381, 1015
Runacres M. C., Owocki S. P., 2005, A&A, 429, 323
Sander A., Hamann W.-R., Todt H., 2012, A&A, 540, A144
Schaerer D., Maeder A., 1992, A&A, 263, 129
Schaerer D., Schmutz W., Grenon M., 1997, ApJ, 484, L153
Schild H. et al., 2004, A&A, 422, 177
Schmutz W. et al., 1997, A&A, 328, 219
Seaquist E. R., 1976, ApJ, 203, L35
Skinner S. L., Güdel M., Schmutz W., Stevens I. R., 2001, ApJ, 558, L113
St.-Louis N., Willis A. J., Stevens I. R., 1993, ApJ, 415, 298
Stanway E. R., Eldridge J. J., 2018, MNRAS, 479, 75
Stecher T. P., 1970, ApJ, 159, 543
Stock D. J., Barlow M. J., Wesson R., 2011, MNRAS, 418, 2532
Storey P. J., Sochi T., Badnell N. R., 2014, MNRAS, 441, 3028
Sundqvist J. O., Owocki S. P., Puls J., 2018, A&A, 611, A17
Tayal S. S., 2000, ApJ, 530, 1091
van der Hucht K. A. et al., 1996, A&A, 315, L193
van Leeuwen F., 2007, A&A, 474, 653
Weaver T. A., Woosley S. E., 1993, Phys. Rep., 227, 65
Williams P. M., van der Hucht K. A., Sandell G., The P. S., 1990, MNRAS, 244, 101
Williams P. M., Crowther P. A., van der Hucht K. A., 2015, MNRAS, 449, 1834
Wright E. L. et al., 2010, AJ, 140, 1868
York D. G., Rogerson J. B. J., 1976, ApJ, 203, 378

APPENDIX A: FAR-UV SPECTROSCOPY OF γ VEL

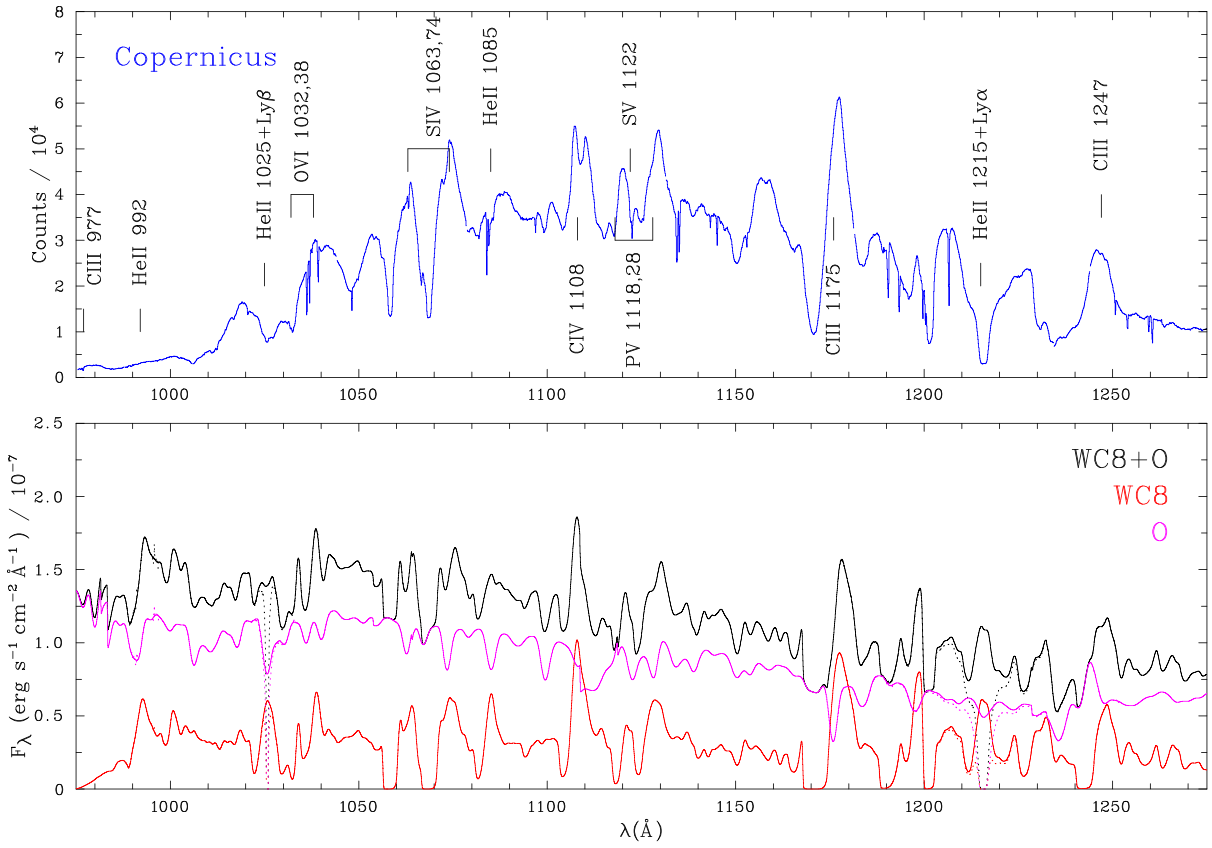

Figure A1. (Top panel): Far-UV uncalibrated *Copernicus* U2 spectroscopy of γ Vel covering $\lambda\lambda$975–1275 (blue), with longer wavelength data sets presented by Johnson (1978); (Bottom panel): Theoretical WC8+O (black), WC8 (red), and O (pink) models, with interstellar Ly α, β excluded (included in dotted lines for $\log(N_{\rm H\,I}/{\rm cm}^{-2}) = 19.8$ (Bohlin 1975; York & Rogerson 1976).

APPENDIX B: γ VEL IONIZATION STRUCTURE

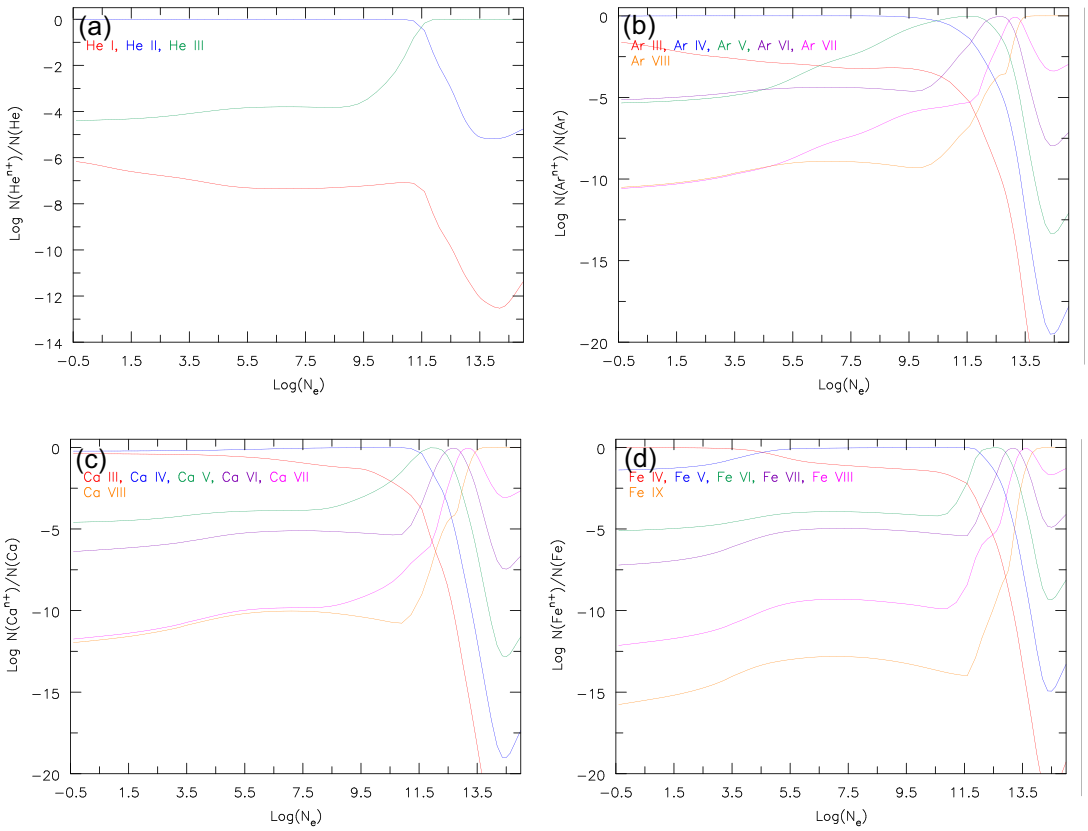

Figure B1. WC8 wind structure for $\log N_e$ (cm^{-3}) versus ionization structure of (a) helium: log He^0/H (red), He^+/He (blue), He^{2+}/He (green); (b) argon: log Ar^{2+}/Ar (red), Ar^{3+}/Ar (blue), Ar^{4+}/Ar (green), Ar^{5+}/Ar (purple), Ar^{6+}/Ar (pink), Ar^{7+}/Ar (orange); (c) calcium: log Ca^{2+}/Ca (red), Ca^{3+}/Ca (blue), Ca^{4+}/Ca (green), Ca^{5+}/Ca (purple), Ca^{6+}/Ca (pink), Ca^{7+}/Ca (orange); (d) iron: log Fe^{3+}/Fe (red), Fe^{4+}/Fe (blue), Fe^{5+}/Fe (green), Fe^{6+}/Fe (purple), Fe^{7+}/Fe (pink), Fe^{8+}/Fe (orange). Higher ionization stages will dominate optically thick regions at high densities ($\log N_e \geq 13.5$).

This paper has been typeset from a TEX/LATEX file prepared by the author.